# Theoretical Studies of the O($^3$P) + Methane Reaction†

**Diego Troya,‡ Ronald Z. Pascual,§ and George C. Schatz*,‡**

*Department of Chemistry, Northwestern University, 2145 Sheridan Road, Evanston, Ilinois 60208-3113, and Department of Chemistry, CAS-University of Southern Mindanao, Kabacan, Cotabato, Philippines 9407*

*Received: January 6, 2003; In Final Form: April 13, 2003*

The dynamics of the O($^3$P) + $CH_4$ reaction has been studied using the quasiclassical trajectory method in conjunction with direct dynamics electronic structure calculations. Several electronic structure methods were used, including DFT (B3LYP/6-31G*) and semiempirical (PM3 and MSINDO) methods. In addition, a recently developed analytical surface (PES) was considered. Our calculations have emphasized collision energies of 1−5 eV because of the importance of this energy range in low Earth orbit research. Our calculated cross sections show that at high energies the H elimination channel yielding H + $OCH_3$ is favored over the lowest barrier product (OH + $CH_3$). Analysis of product energy disposal shows OH and $CH_3$ products that are fairly cold, with most of the energy released to translation. On the other hand, $OCH_3$ carries away most of the energy released to the H + $OCH_3$ products. Angular distributions for OH + $CH_3$ are mainly forward scattered, with a shift from sideways to forward as energy is increased. H + $OCH_3$ is predominantly backward scattered (i.e., the H atom scatters forward). Opacity functions reveal a high selectivity toward OH + $CH_3$ for high impact parameters whereas the H + $OCH_3$ channel is dominant at low impact parameters. MSINDO results compare quite well with more accurate B3LYP/6-31G* calculations, noticeably improving over PM3 for most of the dynamics properties studied.

## I. Introduction

Ground-state oxygen atoms are the most abundant species present in low Earth orbit (LEO) conditions.[1] Surfaces of spacecraft orbiting in LEO (∼200−700 km altitude) are thus exposed to a strongly oxidizing environment that results in materials degradation. This effect is particularly enhanced by the high relative velocity between the spacecraft and the atomic oxygen atoms due to orbital motion. In fact the average relative impact energy of oxygen atoms is around 5 eV.[2,3] Recently, experimental simulations of materials erosion in LEO have been made by employing targets ranging from hydrocarbons to polymers.[4 5] Although these experiments have provided very rich information about the reaction dynamics, the fundamentals of the processes taking place at such high energies are unclear. In addition, there is an absence of theoretical modeling because of the complexity and high dimensionality of the systems involved. Therefore, it is interesting to survey how theory can complement experiment in the understanding of materials erosion due to high-energy oxygen atom collisions.

In this paper, we present a theoretical study of a relatively simple system that is intended to provide a fundamental basis for a thorough understanding of materials erosion. We collide fast oxygen atoms with methane, the shortest chain hydrocarbon, and calculate dynamics properties ranging from cross sections to angular distributions. We also use different representations of the potential surface to see the relationship between accuracy and computation time and to consider the prospect for future studies of higher-dimensionality systems.

O($^3$P) + $CH_4$ is also of interest because of its importance in combustion chemistry as an initial step in hydrocarbon oxidation;[6] therefore, it has been intensively studied over the years at lower energies than those relevant to LEO. Experimental measurements of rate constants for the O($^3$P) + $CH_4$ → OH + $CH_3$ reaction have been available for a long time over a broad temperature range, and the rate constant values can be regarded as well established.[7,8] (For a review, see ref 9.) Experimental studies devoted to the O($^3$P) + $CH_4$ → OH + $CH_3$ reaction dynamics have used translational energies barely above the barrier and have reported energy release to the umbrella mode of the $CH_3$ product[10] as well as OH rovibrational distributions.[11,12]

There is also a wealth of theoretical studies of the O($^3$P) + $CH_4$ → OH + $CH_3$ reaction, including extensive ab initio studies, that have been conducted using ever-increasing levels of accuracy.[13−16] Following most of these detailed ab initio studies, thermal rate constants have been calculated using variational transition-state theory (VTST).[14 15 17] Using VTST and reparametrizing the analytical potential energy surface (PES) of Jordan and Gilbert for the closely related H + $CH_4$ reaction,[18] Espinosa-García et al. were able to derive a full-dimensional PES for the title reaction that reproduced quite accurately the experimental rate constants for O($^3$P) + $CH_4$ → OH + $CH_3$.[17]

Theoretical studies of reaction dynamics include three-[15,19] and four-dimensional[20−23] calculations that have revealed many aspects of the reaction dynamics, ranging from rate constants to angular distributions, but always involving a relatively low translational energy. Furthermore, improvement in the quantum dynamics algorithms has recently led to the first full-dimensional quantum dynamics study of the cumulative reaction probabilities and rate constants for the O($^3$P) + $CH_4$ → OH + $CH_3$ reaction.[24] These accurate rate constants based on the PES of ref 17 were in excellent agreement with VTST results on the same PES, confirming the sufficiency of VTST to predict accurate rate constants.

Full-dimensional calculations of properties other than rate constants for O($^3$P) + $CH_4$ → OH + $CH_3$ or studies of product

† Part of the special issue "Charles S. Parmenter Festschrift".

* To whom correspondence should be addressed. E-mail: schatz@chem.nwu.edu.

‡ Northwestern University.

§ CAS-University of Southern Mindanao.

10.1021/jp034027r CCC: $25.00 
Published on Web 06/13/2003

**TABLE 1: Reaction Energies of the Different Stationary Points Involved in the $O(^3P) + CH_4$ Reaction[a,b]**

| | PES | PM3 | MSINDO | B3LYP/ 6-31G* | CCSD(T)[c]/ AUG-cc-pVTZ | exptl[d] |
|---|---|---|---|---|---|---|
| $OH(^2\Pi) + CH_3(^2A_2'')$ | 0.095(0.222) | −0.876(−0.683) | −0.342(−0.151) | 0.276(0.472) | 0.152(0.288) | 0.11 |
| $H(^2S) + OCH_3(^2A')$ | 1.878(2.219) | −0.446(−0.213) | 0.081(0.284) | 0.540(0.769) | 0.778(0.950) | 0.62 ± 0.04 |
| $CH_2O(^1A_1) + 2H(^2S)$ | | 0.498(1.022) | 1.513(2.034) | 1.621(2.122) | 1.643(2.107) | 1.59 |
| $CHO(^2A') + H(^2S) + H_2(^1\Sigma_g^+)$ | | −1.367(−0.782) | 0.150(0.779) | 0.846(1.444) | 0.940(1.499) | 0.88 ± 0.04 |
| $CH_2OH(^2A) + H(^2S)$ | | −1.095(−0.840) | −0.124(0.110) | 0.517(0.726) | 0.412(0.576) | 0.30 ± 0.04 |
| $O-H-CH_3$ ($^3A''$) | 0.425(0.563) | 0.304(0.469) | 0.564(0.699) | 0.305(0.485) | 0.497(0.635) | |
| $O-CH_3-H$ ($^3A''$) | 1.897(2.184) | 1.104(1.180) | 1.869(1.986) | 1.852(2.006) | 2.096(2.204) | |

[a] Energies referred to the $O(^3P) + CH_4$ asymptote in eV. [b] Energies in parentheses indicate classical energies (i.e., without zero-point energies). [c] CCSD(T)/AUG-cc-pVTZ single-point calculations using UMP2/AUG-cc-pVDZ optimized geometries and frequencies. [d] $\Delta H_{298K}$ obtained from the experimental heats of formation.[38]

channels other than $OH + CH_3$ are, however, unavailable. In the present study, we use full-dimensional trajectory calculations to study the title reaction over a broad range of translational energies and particularly focusing on high (several electronvolts) energies. In addition, our study will emphasize the use of direct dynamics (i.e., on-the-fly) electronic structure methods that will enable us to describe all of the relevant product channels that are open at the initial conditions considered.

The paper is structured as follows: section II gives computational details, section III presents the results, and section IV summarizes the conclusions.

## II. Computational Details

We have used the quasiclassical trajectory method to study the $O(^3P) + CH_4$ reaction dynamics. Although quantum schemes have been applied to study the $O(^3P) + CH_4 \rightarrow OH + CH_3$ reaction dynamics,[20−23] they have always involved reduced dimensionality approximations that may obscure the dynamics behavior of the degrees of freedom that are not included in the treatment. Moreover, the high energies involved in the present study would require computational resources for quantum dynamics calculations that are prohibitive at the moment and probably unnecessary for the purposes of this paper. The characterization of product channels other than $OH + CH_3$ would also require serious algorithm improvements for quantum calculations, so full-dimensional quasiclassical calculations are the only practical approach available for the present full-dimensional dynamics studies.

The potential energy and gradients for these calculations come from four different sources. In the first, we use an analytical PES derived in ref 17, which has been shown to give accurate rate constants for the $O(^3P) + CH_4 \rightarrow OH + CH_3$ reaction.[24] The other three sources involve "direct dynamics" calculations in which electronic structure calculations are performed on the fly while the trajectory is evolved. The three electronic structure methods that are used are (1) PM3 semiempirical calculations[25] as coded in the GAMESS package of programs,[26] (2) a more recent semiempirical Hamiltonian termed MSINDO,[27−29] and (3) density functional theory (DFT) calculations (B3LYP/6-31G*).[30,31] Of these three electronic structure models, the DFT approach provides the highest level of theory that we have used for direct dynamics, with likely errors of 3−4 kcal/mol that are much smaller than the available energies. It is not known which of the two semiempirical approaches is more accurate, but we will study this point later. In all cases, we used unrestricted wave functions. Spin contamination has been reported to be small (2.4% deviation of the exact expectation value of the squared spin operator $\langle S^2 \rangle$) for the abstraction saddle point.[16] We find analogous values in our unrestricted B3LYP and MSINDO calculations. Because in our dynamics studies we are going to be interested in regions of the surface that are much higher in energy than the abstraction saddle point, we have studied the spin contamination for higher-energy saddle points. B3LYP deviations from the expected value (2.0) of $\langle S^2 \rangle$ in high-energy saddle points were never larger than 1.5%. Spin contamination in UMP2 and MSINDO wave functions was a little bit larger, with maxima in the deviations of 5.5 and 4.9% respectively.

All of the calculations refer to the lowest potential energy surface ($1^3A$ surface in $C_1$ symmetry). However, the first excited surface ($2^3A$ in $C_1$ symmetry) exhibits a saddle point for abstraction or addition that is very close in energy to the lowest surface, and although both surfaces differ when moving away from these reaction pathways, the two surfaces likely have a comparable effect on the dynamics at the energies that we are considering. Indeed, reactive scattering calculations performed by two of us on the $^3A''$ and $^3A'$ potentials[32] of $O(^3P) + H_2$ have revealed that dynamics properties such as angular distributions or product energy release are nearly coincident for both surfaces.[33] In the title reaction, the two lowest triplet surfaces are degenerate for collinear approaches. However, Jahn−Teller distortion splits the surfaces, generating two abstraction saddle points ($^3A''$ and $^3A'$) of $C_s$ symmetry. Our calculations on the H-abstraction and H-elimination saddle points refer to the lowest-energy $^3A''$ states. Likewise, $OCH_3$ shows Jahn−Teller distortion from $C_{3v}$ symmetry that splits the $^2E$ state into two states ($^2A'$ and $^2A''$) of $C_s$ symmetry.[34] All of our calculations refer to the methoxy ground state ($^2A'$).

In Table 1 , the energetics of the more important stationary points for $O(^3P) + CH_4$ are compared for the four potential surfaces used in the reaction dynamics studies. Also presented are energies from more accurate CCSD(T)[35]/AUG-cc-pVTZ[36]//UMP2(FULL)/AUG-cc-pVDZ ab initio calculations for which, together with B3LYP/6-31G*, we have used the QChem program.[37] The coupled-cluster calculations are supposed to be accurate to within 0.05 eV with respect to the experiments,[38] and indeed the results in the Table show this level of comparison. CCSD(T) calculations on $H + OCH_3$ seem to deviate more than expected from experiment, and it should be noted that basis set incompleteness could also play a role. We also see that the analytical PES of ref 17 provides an $OH + CH_3$ reaction energy and barrier within 0.05 eV of our CCSD(T) calculations. This high accuracy is not surprising given that this PES was calibrated so as to reproduce experimental rate constants for the $O(^3P) + CH_4 \rightarrow OH + CH_3$ channel. However, we see that the reaction energy for the $OCH_3 + H$ channel is highly overestimated because of the fact that this channel was not considered in the reparametrization of the $HCH_4$ PES[18] to study $O(^3P) + CH_4$. PM3 calculations exhibit a larger exothermicity than experiment for most of the reaction products, and the two barriers that are calculated are in both cases too small.

These deviations between PM3 calculations and more accurate calculations are well known, and there have been several efforts to reparametrize the PM3 Hamiltonian to fit the energy profiles of specific reactions.[39,40] As an alternative to reparametrizing the original PM3 Hamiltonian, we will examine results for the semiempirical MSINDO Hamiltonian. Table 1 shows that the MSINDO reaction energies are noticeably closer to more accurate calculations than the respective PM3 values. For the two major channels ($OH + CH_3$ and $OCH_3 + H$), the MSINDO deviations from CCSD(T) values are about half of the error associated with PM3. The B3LYP/6-31G* calculations show expected deviations (0.1−0.2 eV) with more accurate calculations and, except for the H abstraction barrier height, fair improvement over semiempirical results. Thus, apart from the analytical PES, the sequence in accuracy of the electronic structure methods employed in this work is PM3 < MSINDO < B3LYP/6-31G* < CCSD(T)/AUG-cc-pVTZ. However, when dealing with direct dynamics, the computation time dramatically constrains the electronic structure method that can be used for the energy-gradient evaluation at each integration step of the trajectories. In this way, the preferred sequence for performing direct dynamics calculations in this work would be CCSD(T) < B3LYP/6-31G* < MSINDO ≈ PM3. This sequence is illustrated by the following relative CPU times for the calculation of energy gradients for an arbitrary point of the $OCH_4$ ground-state surface in increasing order of accuracy: $1 \approx 1{:}2200{:}4.3 \times 10^6$ (where the CCSD(T) ratio is estimated on the basis of single-point energies). This means that PM3 trajectories are about as fast as MSINDO and orders of magnitude faster than the more accurate methods. Indeed, it is impossible for us to perform direct dynamics with coupled-cluster methods, and even with DFT, the number of integrated trajectories is limited (a few hundred). Trajectories employing the analytical potential energy surface are about 1 order of magnitude faster than PM3. Given the comparisons of accuracy and computation time, it will be interesting to pay particular attention to MSINDO as a novel method for improved accuracy dynamics calculations on large systems.

We have used the leapfrog algorithm embedded in GAMESS[41] to solve the equations of motion for the PM3 and B3LYP/6-31G* calculations. For the analytical PES and MSINDO calculations, we have used a standard fifth-order predictor, sixth-order corrector integrator that has been widely employed in previous calculations of our group.[42,43] The initial conditions of methane are prepared using normal-mode sampling. The integration step for the PES and B3LYP/6-31G* calculations was 5.0 au, that for PM3 was 2.5 au, and the integration step for MSINDO was set to 10 au after verifying that smaller integrations steps did not improve total energy conservation. Energy is conserved to four or more figures in most of the calculations.

For the analytical PES, we have run batches of 50 000 trajectories per translational energy. This number was reduced to about 10 000 trajectories for PM3 and MSINDO and to roughly 500 for B3LYP/6-31G*. These figures reflect the differences in computation time of the different methods as well as the size of the error bars associated with the dynamics properties presented. Trajectories are started at a distance of 12 au between the impinging oxygen atom and the methane center of mass in PES, PM3, and MSINDO calculations. We had to reduce this distance to about 8 au for B3LYP calculations because of the poor SCF convergence of the DFT wave function for large atom−molecule separations, likely because of the degeneracy of the two lowest-energy triplet surfaces that correlate to $O(^3P) + CH_4$.

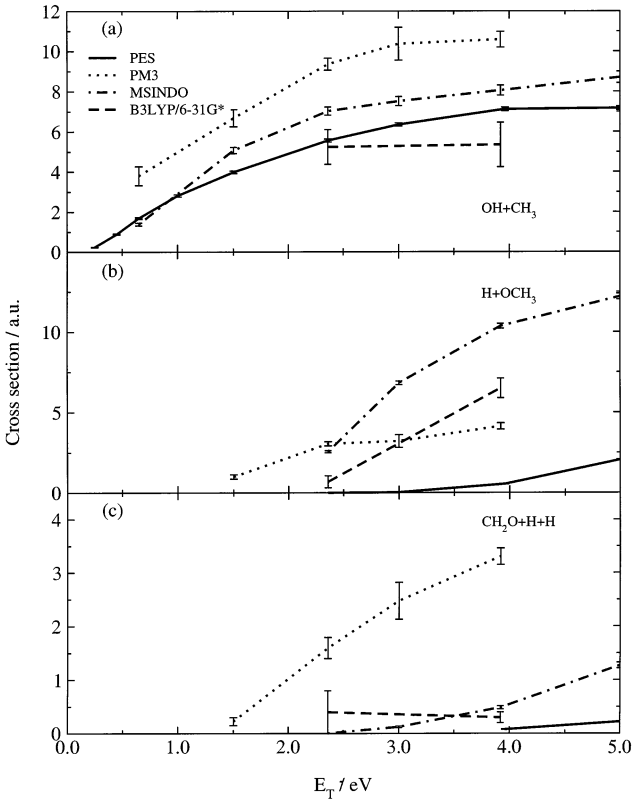


**Figure 1.** Excitation functions for the $O(^3P) + CH_4$ reaction. (a) $OH + CH_3$ products. (b) $H + OCH_3$ products. (c) $CH_2O + 2H$ products.

To make contact with LEO experiments, we have paid particular attention to high-energy (several electronvolts) collisions. Oxygen atoms (5 eV) colliding with methane imply a relative translational energy of about 2.5 eV to the center of mass. Because of the enormous requirements in computing time when using B3LYP/6-31G* calculations, we have constrained our B3LYP calculations to a relative translational energy close to 2.5 eV (2.36 eV) and to a higher energy (3.92 eV) that is representative of the high-energy wing of the oxygen atom translational energy distribution in LEO.

## III. Results

**III.1. Excitation Functions.** Figure 1 depicts the excitation functions (cross sections vs translational energy) of the three most important product channels. The cross sections for $OH + CH_3$, which involves reaction over a relatively small barrier, show the customary dependence on energy for reactions with a threshold. The cross sections increase from the threshold to a maximum at around 5 eV and then slightly decrease or are constant at higher energy. All of the four potential energy functions show peak cross sections that are within a factor of 2. PM3 seems to overestimate reactivity, whereas the deviation of the rest of the calculations from each other is smaller. The MSINDO results are somewhere between PM3 and B3LYP, indicating, in agreement with Table 1, that MSINDO is a more accurate method than PM3. The agreement between the high-energy PES and MSINDO or DFT cross sections is also remarkable given that the analytical PES was optimized to match measured thermal rate constants. Whereas low-temperature rate coefficients are primarily dependent on the size and shape of the minimum-energy reaction path (MEP), the high-energy cross sections are not expected to show a strong dependence on the

features of the MEP. However, the MEP calibration of the PES based on thermal rate constants seems to be rather suitable for more repulsive regions of the surface as well.

Although we are not emphasizing the behavior of cross sections near the threshold in this paper, it is noteworthy that the thresholds in Figure 1a are well below the zero-point-corrected barrier heights in Table 1. For example, for the PES surface, the effective threshold in Figure 1 (extrapolating the low-energy cross section to zero) is at about 0.2 eV, whereas the zero-point-corrected barrier is 0.4 eV. The large difference between these two results indicates significant nonadiabatic behavior in the QCT results. Although small negative deviations from the adiabatic threshold are possible, the large deviations seen here are likely an important error in the QCT results. Although this problem is known for simpler reactions such as atom−diatom reactions, the fortuitous cancellation between tunneling and nonadiabaticity that often occurs for these reactions likely does not occur in the present case.

Figure 1 shows that the $OCH_3 + H$ product channel has a significant cross section at collision energies above 2 eV. This product has not been considered in earlier studies of $O(^3P) + CH_4$ probably because Table 1 indicates that it is about 0.5 eV more endoergic than $OH + CH_3$. The PM3 result in Figure 1 has the lowest threshold, corresponding to the lowest reaction barrier. MSINDO and B3LYP/6-31G* show similar behavior, and the level of agreement between them is comparable to that for the $OH + CH_3$ products with the MSINDO cross sections slightly overestimating the B3LYP calculations. The PES cross sections are, not surprisingly, very small compared with those from the rest of the methods. This is a consequence of the absence of calibration of this channel in the PES construction. MSINDO seems again to be a more reliable technique than PM3, providing an excitation function that is in closer agreement with B3LYP/6-31G* calculations than PM3 for most of the interval of translational energies considered.

Interestingly, whereas at 2.36 eV the $OH + CH_3$ cross section is larger than that for $OCH_3 + H$, the latter channel is dominant at higher energy. This has important implications in the LEO experiments because oxy radical formation provides a direct pathway for the formation of CO and $CO_2$. In addition, this result shows that under LEO conditions oxygen atom reactions with a polymeric hydrocarbon are likely to give products other than that with the lowest-energy barrier. This is consistent with very recent LEO experimental simulations carried out by Minton and co-workers in which products other than OH were observed coming off hydrocarbon polymeric surfaces under LEO conditions.[44]

$CH_2O + 2H$ is a product that is also observed in all calculations. PM3 seems to overestimate the reactivity associated with this channel, as expected from the underestimated endothermicity (Table 1). The other potential surfaces show a small cross section that increases slowly with translational energy. The MSINDO and B3LYP/6-31G* results are also in agreement in the range of translational energies explored. We also observe traces of $CH_2OH + H$ and $CHO + H + H_2$, but the cross sections are almost negligible and have been omitted.

**III.2. Product Energy Distributions.**

**III.2.A. OH + $CH_3$.** Measurements of product energy distributions for the $O(^3P) + CH_4 \rightarrow OH + CH_3$ reaction have been reported both for the nascent OH rovibrational distributions[11] and the $CH_3$[10] vibrational distributions. McKendrick and co-workers photodissociated $NO_2$ at 248 nm to generate $O(^3P)$ atoms with an average translational energy in the $(O + CH_4)$ center of mass of 0.348 eV.[11] In another experiment, oxygen atoms were generated by Suzuki and Hirota using $SO_2$ photolysis at 193 nm, thereby yielding a translational energy of about 0.330 eV.[10] The translational energy distributions are very broad in both cases, and even though the peak of the distributions lies below the adiabatic barrier to reaction (0.4 eV), reaction is still possible from the high-excitation tails of the energy distribution. This implies that the energy disposal to products is going to be strongly dependent on features of the minimum-energy reaction path. From a theoretical standpoint, mimicking these experiments is a rather complicated task because the translational energy is not unique and an accurate representation of the MEP is needed. Computational limitations have forced us to choose a translational energy of 0.65 eV and to use the two less-expensive techniques considered here (PM3 and MSINDO) together with the analytical potential energy surface. Fortunately, $E_{coll} = 0.65$ eV corresponds to the low-vibrational excitation peak in the NO distribution emerging from the $NO_2$ photodissociation at 248 nm;[45] therefore, this energy is expected to be representative of the high-excitation tail of the translational-energy distribution of the McKendrick experiment.

In the experiments, OH was found to be cold, with no excitation in $OH(v' = 1)$, and a rotational $OH(v' = 0)$ distribution peaking at $N' = 2$.[11] The $\nu_2$ mode in $CH_3$ (out-of-plane bending "umbrella" mode) was also observed to be cold but slightly more excited than that predicted by a prior population analysis.[10] Our calculations using the available analytical PES at 0.65 eV give vibrationally cold OH ($P(v' = 0)/P(v' = 1) = 0.82 \pm 0.05{:}0.18 \pm 0.03$) although more excited than in the experiments. The difference between theory and experiment could arise from several sources, including problems with zero-point violation, the somewhat higher energy of the QCT simulations compared to experiment, problems with the use of rounding off to define product quantum numbers, and of course errors in the potential energy surface. As a test of the last point, we see that the MSINDO calculations are in good agreement with the PES numbers, giving $P(v' = 0)/P(v' = 1) = 0.93 \pm 0.05{:}0.07 \pm 0.02$, although closer to experiment. However, PM3 calculations show an inverted vibrational distribution, $P(v' = 0)/P(v' = 1)/P(v' = 2)/P(v' = 3) = 0.0 \pm 0.0{:}0.31 \pm 0.03{:}0.62 \pm 0.04{:}0.07 \pm 0.02$, in stark disagreement with experiment and the other calculations.

In contrast to the cold vibrational distributions found in most simulations, the OH rotational distributions are noticeably more excited in all of the calculations than in the experiments. The $OH(v' = 0)$ rotational distribution calculated with the analytical PES peaks at $j' = 13$ and states up to $j' = 20$ are populated. MSINDO's $OH(v' = 0)$ peak occurs at $j' = 15$. There is no population in $OH(v' = 0)$ for PM3, and that for $OH(v' = 1)$ peaks at $j' = 11$. As with the vibrational distributions, the discrepancy with experiment can arise from several sources, although here the rounding-off algorithm used to define quantum numbers is probably not important. We have studied other possible explanations by making additional calculations at lower translational energy. We find that reducing the translational energy and reducing the reagent vibrational energy both lead to a reduction in the OH rotational energy, although in no case does the product OH rotational distribution peak drop below $j' = 10$. Thus, we infer that the accuracy of the potential energy surface is also involved.

To verify the influence of the potential on the product OH rotational excitation, we should bear in mind that OH rotation is going to be very dependent on the value of the C−H−O bending frequency close to the transition state. $O(^3P) + CH_4 \rightarrow OH + CH_3$ can be modeled as having heavy−light−heavy

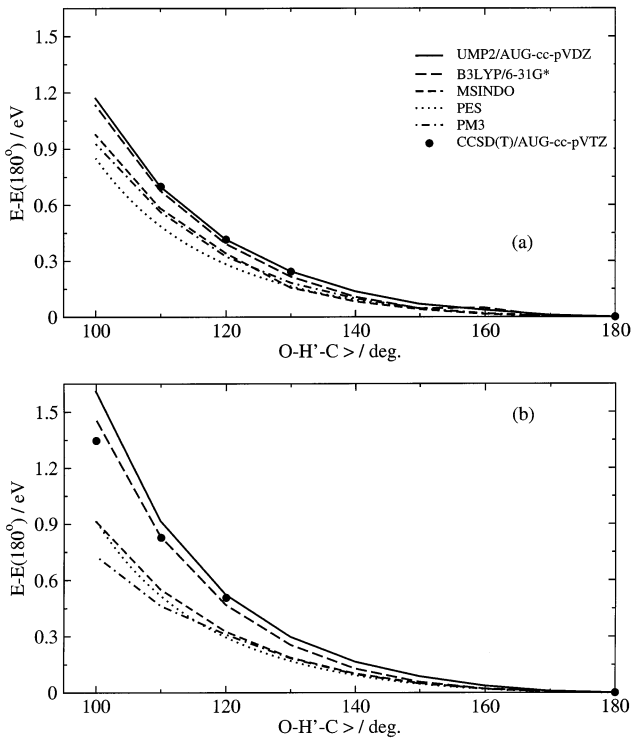


**Figure 2.** Saddle point C−H′−O bending-energy curves for the O($^3$P) + $CH_4$ → OH′ + $CH_3$ reaction. (a) H−C−H′−O dihedral angle = 180°. (b) H−C−H′−O dihedral angle = 0°. The values of the remaining coordinates correspond to the saddle point values for the respective methods. See the text.

kinematics (H−L−H). Earlier work carried out on the H−L−H benchmark triatomic reaction Cl + HCl → HCl + Cl[46] showed a remarkable correlation between the saddle point bending frequency and the product HCl rotational distributions such that surfaces with the same saddle point but a different dependence of the energy on the bending angle showed very different rotational excitation in the HCl product (with tighter bends yielding colder rotations). Inspired by this, we have carried out quantum chemistry calculations of the C−H′−O bending-energy curves (with H′ being the hydrogen atom abstracted) for the different potentials used in this work. Thus, we fix all coordinates except the C−H′−O bending angle and the H−C−H′−O dihedral angle (H being the hydrogen atom not abstracted, which is different from the other two by the Jahn−Teller effect) to the values of the respective saddle points. Figure 2 shows the bending curves for the various methods used here for two different H−C−H′−O dihedral angles: (a) $\phi = 180°$ and (b) $\phi = 0°$. The latter, 0°, represents the situation in which the newly formed O−H′ bond is directly facing one nonreactive C−H bond, whereas for 180° the O−H′ bond lies between the other two C−H bonds. The bending curves for $\phi = 180°$ in Figure 2a show DFT and ab initio energies that are in good agreement with each other and more repulsive than the energies from semiempirical methods and the PES. The differences are much exaggerated for $\phi = 0°$, where the DFT or ab initio curves show much higher anisotropy than the rest of the calculations. It is remarkable that whereas the DFT and ab initio calculations show repulsive interactions between the electron pairs of the O−H′ and C−H bonds for $\phi = 0$ and 180° the semiempirical calculations fail to describe this. Indeed, MSINDO and PM3 predict that the $\phi = 0°$ approach is more favorable than the $\phi = 180°$ approach. The analytical PES curves for both dihedral angles mostly overlap with each other, and for a 100° bending angle, the energy of the $\phi = 0°$ arrangement is 0.065 eV above that of the $\phi = 180°$ arrangement.

This has clear implications for OH rotational excitation because looser saddle points imply broader cones of acceptance, allowing C−H′−O angles further from the collinear minimum-energy path, which translates into larger OH product rotational excitation. And this is what we see in our low collision energy calculations when compared with experiment.

However, B3LYP energy values show the correct anisotropy when compared with higher-level calculations. Unfortunately, direct dynamics B3LYP/6-31G* at low collision energy compared with experiments are prohibitive at the moment. What we learn from this comparative study is that OH rotation is a more demanding dynamics property than vibration in assessing the accuracy of the surface. Although the MSINDO, PM3, and PES potentials furnish reasonable values for the reaction barrier, the saddle point bending mode is looser than it should be, and this leads to excessive OH rotational excitation.

Regarding energy released to $CH_3$ at $E_{coll} = 0.65$ eV, we find that the PES and MSINDO results show internal energies between 4 and 5 kcal/mol below the methyl zero-point energy (ZPE), whereas the PM3 calculations yield results around 1 kcal/mol above the ZPE. Zero-point energy violation is a well-known flaw associated with quasiclassical trajectory calculations, and it is particularly important for molecules containing a large number of vibrational degrees of freedom, such as methyl. In addition, there are no algorithms available that properly perform quantization of the vibrational states of molecules larger than three atoms and that can be used at the end of a quasiclassical trajectory calculation to determine final-state distributions. As a result, an analysis of which modes violate zero-point energy cannot be made at this time. Irrespective of this, we see that there is little energy released to the methyl group under these conditions, suggesting the validity of the often-invoked triatomic model in which the degrees of freedom of the methyl group are eliminated.[15,19,47,48]

Because the main interest of this paper lies in the characterization of the reaction dynamics at higher energies due to interest in structural damage in LEO, some of the problems just discussed can be ignored. In Figure 3, we have plotted the average fractions of energy in the OH + $CH_3$ products as a function of translational energy for the different potential surfaces employed in this work. We note that to make contact with experiment, zero-point energy has been subtracted in calculating the results. This means that the available energy is $E_{coll} + \Delta H + \mathrm{ZPE}(CH_4) - \mathrm{ZPE}(CH_3) - \mathrm{ZPE}(OH)$. However, as often occurs when doing quasiclassical trajectory calculations, $CH_3$ or OH products are sometimes generated with vibrational energies below their zero points (i.e., the zero-point energy is violated). This implies negative fractions of energy that obviously do not have any physical meaning. To avoid this, whenever OH or $CH_3$ products emerge with energy lower than their zero point, the fraction of energy released to these modes is considered to be zero, and the available energy is renormalized so that the remaining fractions of energy add up to 1.

Figure 3a shows the energy release to translation. The fractions of translational energy increase abruptly with collision energy at low energies, becoming somewhat constant at higher energies, so that at high energies product translation receives most of the total energy available. When the large uncertainties in our DFT calculations are accounted for, the B3LYP/6-31G* and MSINDO values show good agreement, with PES also in fair agreement and PM3 noticeably underestimating the rest of the calculations.

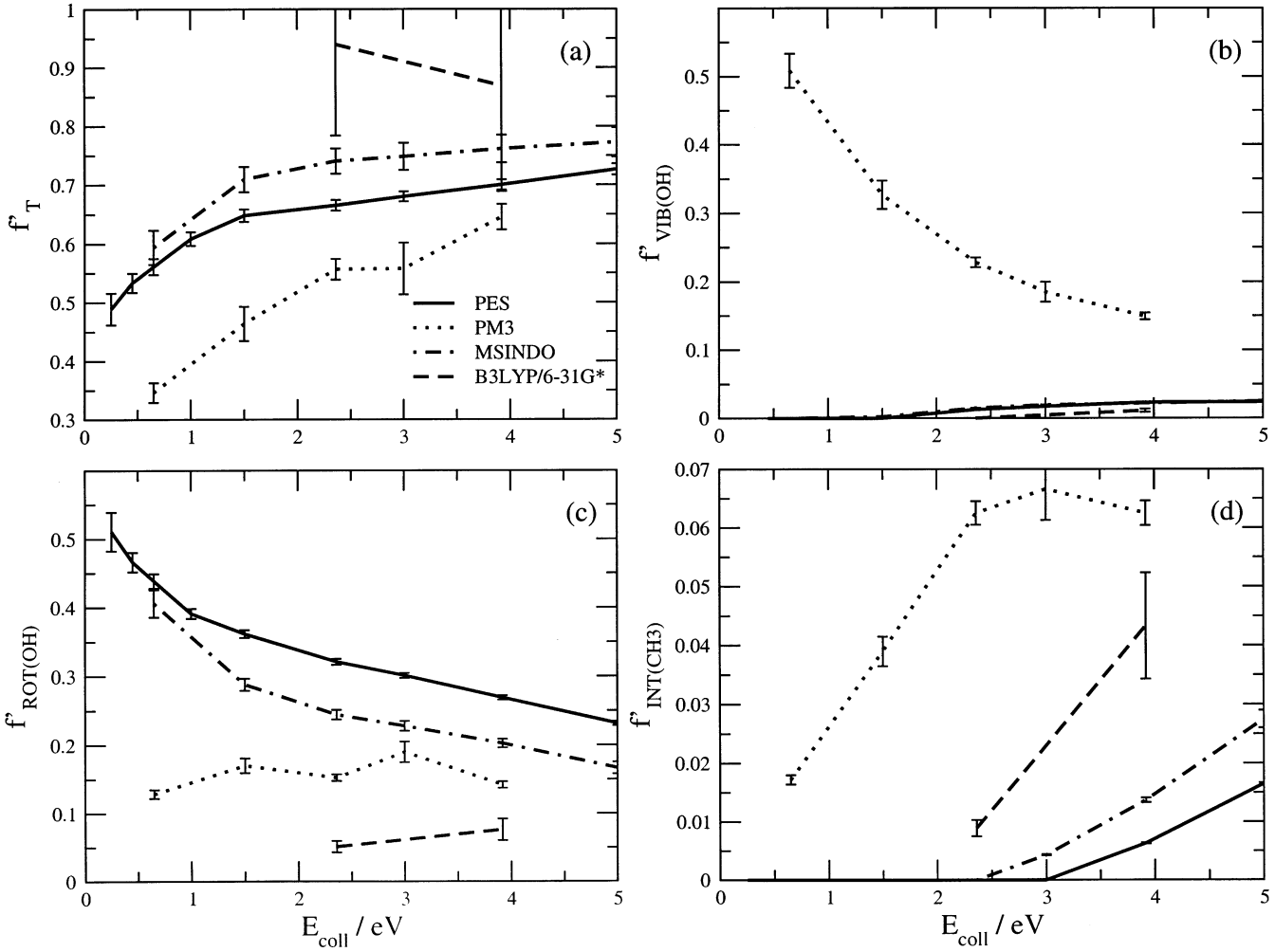


**Figure 3.** Energy release in terms of the average fraction of the available energy appearing in a specified degree of freedom for the $O(^3P) + CH_4 \rightarrow OH + CH_3$ reaction. (a) Average fraction in translational energy. (b) Average fraction in OH vibrational energy. (c) Average fraction in OH rotational energy. (d) Average fraction in $CH_3$ internal energy.

An analysis of OH vibration (Figure 3b) reveals the source of disagreement between the different potentials employed in this work. As mentioned above, whereas the OH coming from the PES and MSINDO calculations is cold, PM3 furnishes inverted OH vibrational populations. The more accurate B3LYP calculations support what is predicted by MSINDO and PES. At moderate and high energies, $f'_{vib(OH)}$ increases slowly with translational energy for the MSINDO, B3LYP/6-31G*, and PES calculations, meaning that the increase in OH vibration with translational energy is about as fast as the increase in available energy. PES and MSINDO calculations at low energy also indicate that the average energy available to OH vibration is below the zero point.

Turning our attention to OH rotation, we see in Figure 3c that although all of the methods indicate that less than half of the available energy goes to OH rotation the different electronic structure methods do not agree very well. In particular, the B3LYP/6-31G* result is much lower than the rest, and PES is the highest. This is direct evidence of the different C−H−O bending-energy curves discussed above. The OH fractions in rotation are, for PM3 and B3LYP calculations, only weakly dependent on collision energy, and if the B3LYP/6-31G* result is extrapolated to low energy where experiments resolving the product OH have been performed,[11] this leads to good agreement between theory and experiment. As mentioned above, this suggests that a proper description of these low-energy experiments requires at least the level of accuracy provided by B3LYP/6-31G* calculations. However, tunneling or other quantum effects may also be a concern when making low-energy quasiclassical trajectory calculations, so one needs to be cautious in doing this extrapolation. The PES and MSINDO average fractions of OH rotational energy decrease rapidly with collision energy at low energies and then level off at higher energies.

The fraction of energy released to $CH_3$ (Figure 3d) internal energy is below the zero-point energy for most calculations at low and moderate collision energies, and it increases with translational energy. Although zero-point energy leakage in the quasiclassical trajectory calculations raises questions about the accuracy of the energy values, the trends should be correct, as supported by the four different calculations that all give similar results. The fact that the energy available to the methyl product is about equal to the zero-point energy is evidence of spectator behavior in the reactive dynamics, where the methane internal modes that evolve into methyl modes are uncoupled from the reaction coordinate. Interestingly enough, this appears to happen even at very high collision energies where a spectator model is not necessarily valid.

**III.2.B. H + $OCH_3$.** Now we focus on energy release to the H + $OCH_3$ product. As noted above, this product is not important at low energies, but it is the dominant product at high energies. We consider only two degrees of freedom: product relative translation and the internal energy of $OCH_3$. The average

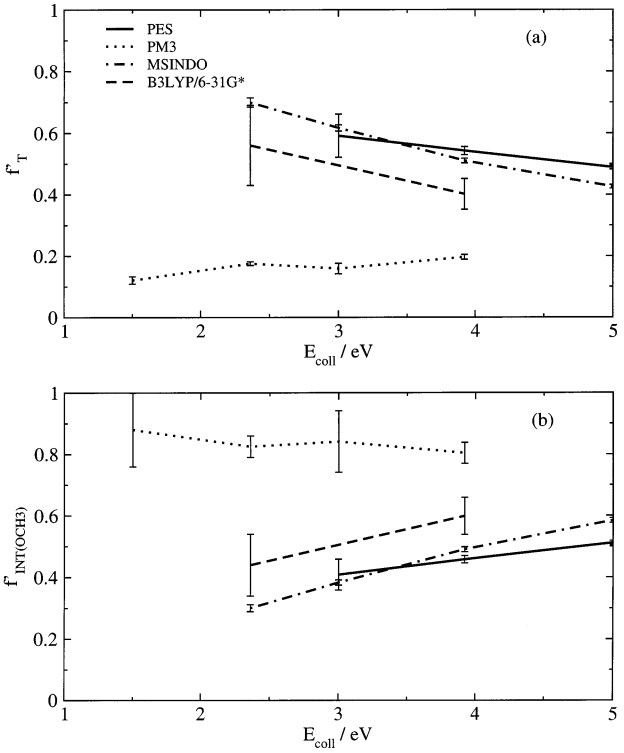


**Figure 4.** Energy release as described in Figure 3 but for the $O(^3P) + CH_4 \rightarrow H + OCH_3$ reaction. (a) Average fraction in translational energy ($f'_T$). (b) Average fraction in $OCH_3$ internal energy ($f'_{int(OCH3)}$).

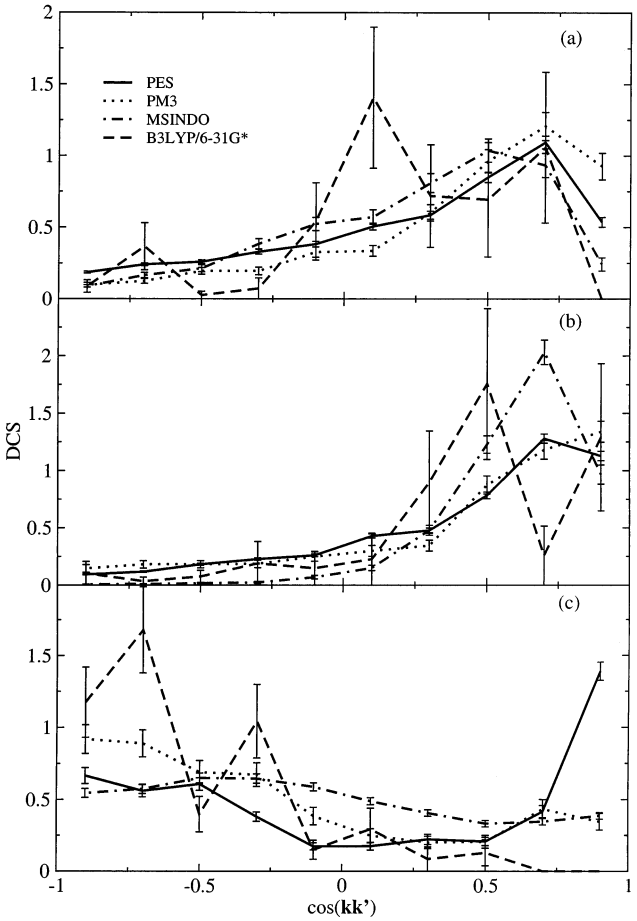


**Figure 5.** Angular distribution expressed as normalized differential cross section (DCS, $(2\pi/\sigma)(d\sigma/d\Omega')$) for the $O(^3P) + CH_4$ reaction calculated using different potential energy surfaces. (a) $O(^3P) + CH_4 \rightarrow OH + CH_3$ with $E_{coll} = 2.36$ eV. (b) $O(^3P) + CH_4 \rightarrow OH + CH_3$ with $E_{coll} = 3.92$ eV. (c) $O(^3P) + CH_4 \rightarrow H + OCH_3$ with $E_{coll} = 3.92$ eV.

fractions of energy as a function of translational energy are depicted in Figure 4. In contrast to $OH + CH_3$, the release to translational energy (Figure 4a) is comparable to the release to internal energy of $OCH_3$ (Figure 4b). Unlike $OH + CH_3$, the polyatomic molecule energy content is well above the zero point. An analysis of excitation in the different vibrational modes would indicate whether energy is retained in the modes that have been formed during the reaction or whether it is shared between the rest of the $OCH_3$ vibrational degrees of freedom, but such an analysis is beyond the scope of this paper. A less quantitative analysis can be made by observing reactive trajectories. Animation reveals that excitation is not confined to the newly formed CO stretch; other modes are also excited. This is in contrast with recent studies of the $OH + D_2 \rightarrow D + HOD$ reaction, where it has been demonstrated that most of the energy released to vibration in HOD goes selectively to the newly formed O−D bond because of the absence of coupling with the rest of the HOD modes.[49,50] Apparently, the multiple low-energy modes in $OCH_3$ allow for energy to flow more freely in the case of $O(^3P) + CH_4$.

The fraction of energy released to the internal degrees of freedom of the polyatomic $OCH_3$ fragment increases with collision energy at the expense of the fraction of energy released to translational energy. At higher energies, the fraction of energy in translation is lower than the fraction of internal energy of the $OCH_3$ product, a trend that is noticeably opposite to that of the $OH + CH_3$ channel.

MSINDO and B3LYP/6-31G* calculations show common trends and reasonable agreement, whereas PM3 calculations show deviations with both of these techniques that are more striking than they are for $OH + CH_3$. Thus, MSINDO clearly improves upon PM3. Although the PES results are closer to the more accurate calculations, the large overestimation of the reaction energy for this channel indicates that the agreement may be fortuitous.

**III.3. Angular Distributions.** Another property of crucial importance to understanding the microscopic reaction mechanism is the angular distribution. Figure 5 shows angular distributions for both majority channels at translational energies relevant to the LEO experiments. The data of Figure 5a corresponds to $OH + CH_3$ products calculated at $E_{coll} = 2.36$ eV. This shows markedly forward distributions with good agreement between PES, PM3, and MSINDO results. The B3LYP distribution is also displayed for the sake of completeness, but the jagged character of the distribution makes it clear that this result has large error bars due to the small number of reactive trajectories. Interestingly, we observe excellent agreement between all of the levels of electronic structure theory used for this property. This implies that the features of the potential that control the scattering are similar for all surfaces.

The agreement of the various theories is maintained for larger translational energies, as can be seen in the angular distributions for $OH + CH_3$ at $E_{coll} = 3.92$ eV in Figure 5b. Forward scattering is slightly enhanced with respect to $E_{coll} = 2.36$ eV, but we defer a discussion of the evolution of angular distributions with translational energy until later.

Angular distributions for the other major product channel, $H + OCH_3$, are plotted in Figure 5c at $E_{coll} = 3.92$ eV. The distributions are quite broad but with more flux scattered into the backward hemisphere. Agreement between the different

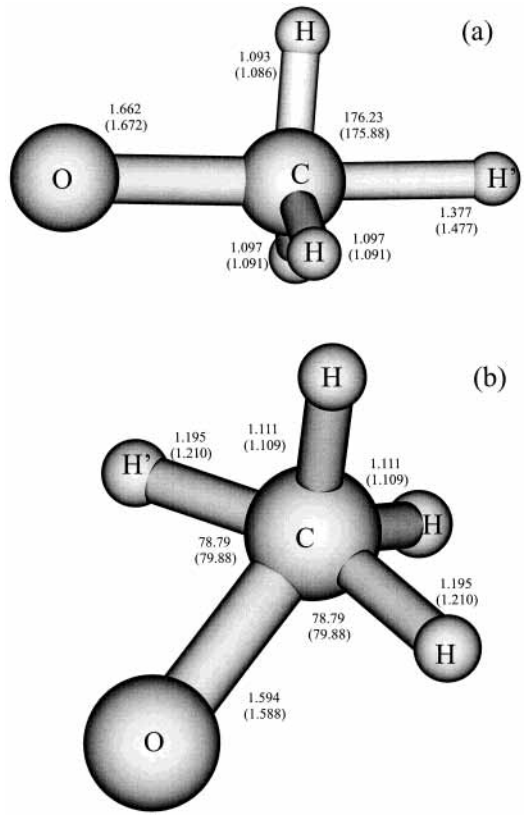


**Figure 6.** Saddle point structures associated with the $O(^3P) + CH_4 \rightarrow H + OCH_3$ reaction. (a) TS1 $SN_2$-like structure. (b) TS2 higher-energy structure. (See the text). Numbers refer to internuclear distances in angstroms and angles in degrees. Plain values correspond to UMP2/AUG-cc-pVDZ calculations, and values in parentheses are for B3LYP/6-31G* calculations.

potentials is not as clear as it is for $OH + CH_3$. The PES results clearly diverge from those of the rest of the theories, showing a spurious forward peak. In the trajectories generating this peak, the exiting hydrogen atom travels in a direction opposite to the incoming oxygen atom, which "squeezes out" that hydrogen atom in its approach. In this mechanism, which has been seen previously for other polyatomic H−L−H model reactions,[51] the system explores regions of the surface that are strongly repulsive in more realistic potentials, giving evidence of flaws in the analytical PES in regions far away from the one to which it was tailored.

Setting aside the PES results, it is somewhat surprising to observe such broad distributions for the $O(^3P) + CH_4 \rightarrow H' + OCH_3$ reaction given its formal similarity with $SN_2$ reactions. For the $SN_2$ mechanism, a nearly collinear O−C−H′ arrangement is expected in the vicinity of the saddle point, with the remaining hydrogen atoms being coplanar with the carbon atom. Motion along the reaction coordinate would then give the exiting hydrogen atom the same direction as the incoming oxygen atom, leading to backward peaked angular distributions. Although the present results show backward character, there is a significant broadening promoted by sideways contributions that imply O−C−H′ angles far from collinearity. To shed light on this issue, we have performed quantum chemistry calculations to characterize the saddle point for H elimination. We find that $H + OCH_3$ can be generated by two distinct reaction mechanisms, each of which has a saddle point. The structures of these saddle points are plotted in Figure 6 , and their harmonic frequencies are reported in Table 2. Saddle point TS1 (Figure 6a) corresponds to the expected $SN_2$-like structure of $C_s$ symmetry, where the incoming oxygen and exiting hydrogen are in a nearly collinear arrangement. Saddle point TS2 (Figure 6b) also leads to H elimination, but in this case, O and H′ form a nearly perpendicular angle, which shows $C_{2v}$ symmetry. All of the energies of the saddle points reported in Table 1 refer to TS1 $SN_2$-like structures that are slightly lower in energy than those corresponding to the $C_{2v}$ TS2 structures. For instance, at the CCSD(T)/AUG-cc-pVTZ//UMP2/AUG-cc-pVDZ level, the energy of saddle point TS2 is 2.509(2.619) eV, about 0.4 eV higher than the TS1 $SN_2$ saddle point (2.096(2.204) eV). B3LYP/6-31G* calculations furnish a TS2 saddle point about 0.3 eV higher in energy than the TS1 saddle point (2.183(2.340) vs 1.852(2.006) eV, respectively). Although the TS2 saddle point is higher in energy, the trajectory calculations reveal that this saddle point and the associated reaction path are dominant at energies well above the threshold. The fact that the B3LYP distributions seem to be more backward than the semiempirical ones may be an indication that the TS2 saddle point is more anisotropic (lower cone of acceptance) in the B3LYP calculations.

Regarding the variation of the angular distributions with collision energy, Figure 7a shows results for the $OH + CH_3$ products for various $E_{coll}$ based on MSINDO calculations. The scattering tends to be more forward with increasing translational energy, following the trend expected for direct reaction mechanisms.[52] This can be noticed by the displacement in the location of the peak toward more forward values of the scattering angle and the diminishing of the flux scattered in the backward hemisphere. Figure 7b shows the respective opacity functions. A clear-cut correlation between the preference for higher impact parameters and more forward scattering can be verified.

**TABLE 2: Harmonic Normal Mode Frequencies of the Saddle Points of the $O(^3P) + CH_4 \rightarrow H + OCH_3$ Reaction[a]**

| TS1 ($C_s$, $^3A''$) B3LYP/6-31G* | TS1 ($C_s$, $^3A''$) UMP2/AUG-cc-pVDZ | TS2 ($C_{2v}$, $^3B_2$) B3LYP/6-31G* | TS2 ($C_{2v}$, $^3B_2$) UMP2/AUG-cc-pVDZ |
|---|---|---|---|
| 3233.8 (A′) | 3266.9 (A′) | 2978.6 ($B_1$) | 3068.6 ($B_1$) |
| 3171.9 (A″) | 3206.1 (A″) | 2880.3 ($A_1$) | 2945.0 ($A_1$) |
| 3046.9 (A′) | 3053.3 (A′) | 1918.4 ($A_1$) | 2092.9 ($A_1$) |
| 1398.8 (A″) | 1426.5 (A′) | 1781.0 ($B_2$) | 2009.3 ($B_2$) |
| 1383.4 (A′) | 1378.2 (A″) | 1466.5 ($A_2$) | 1413.1 ($A_2$) |
| 1347.6 (A′) | 1358.3 (A′) | 1421.7 ($A_1$) | 1407.3 ($B_2$) |
| 1261.7 (A′) | 1284.4 (A′) | 1383.2 ($B_2$) | 1396.1 ($A_1$) |
| 924.7 (A″) | 885.9 (A″) | 1151.9 ($A_1$) | 1117.9 ($A_1$) |
| 702.3 (A′) | 807.4 (A′) | 1123.4 ($B_1$) | 1047.4 ($B_1$) |
| 485.9 (A′) | 509.1 (A′) | 845.4 ($B_2$) | 823.2 ($B_2$) |
| 413.0 (A″) | 306.9 (A″) | 337.0 ($B_1$) | 148.3 ($B_1$) |
| 1418.8i (A′) | 1758.1i (A′) | 982.2i ($A_1$) | 1203.1i ($A_1$) |

[a] Structures of saddle points TS1 and TS2 are presented in Figure 6a and b, respectively.

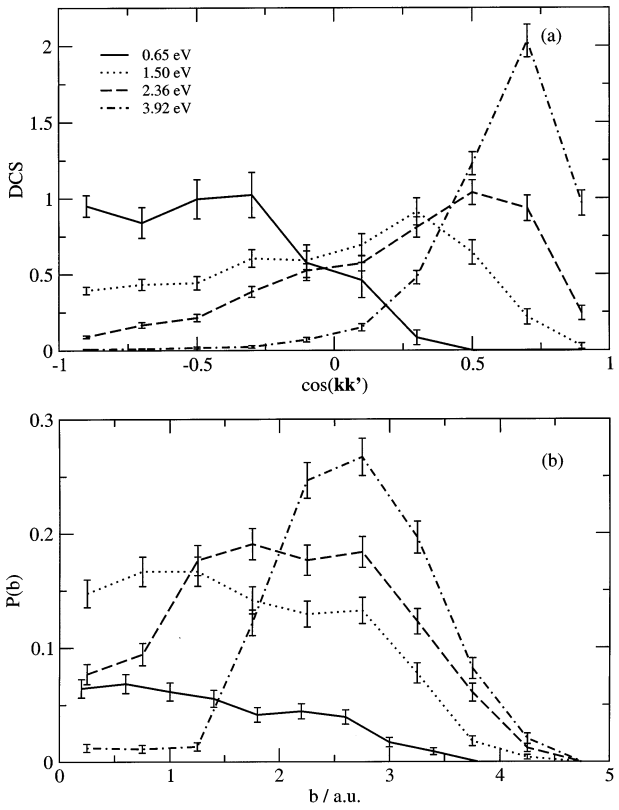


**Figure 7.** (a) Angular distributions for the O($^3$P) + $CH_4$→ OH + $CH_3$ reaction for various translational energies expressed as normalized differential cross sections (DCS, $(2\pi/\sigma)(d\sigma/d\Omega')$). (b) Opacity functions for the O($^3$P) + $CH_4$→ OH + $CH_3$ reaction. Legends are the same as for panel a. All of the calculations correspond to the MSINDO potential energy surface.

Moreover, it is remarkable that at high collision energy there is almost negligible reactivity to give OH + $CH_3$ coming from impact parameters in the range of 0−1.5 au. The analysis of the H + $OCH_3$ channel indicates that most of the low impact parameter reactive trajectories yield this channel instead of OH + $CH_3$. Therefore, the evolution in the OH + $CH_3$ scattering toward more forward scattering with increasing collision energy should be understood not only as a preference for larger impact parameters but also as competition from the H + $OCH_3$ channel for reaction at a low impact parameter.

Lower-energy calculations have also been made to verify that backward distributions are obtained for the OH + $CH_3$ product for energies barely above the threshold where reactive trajectories consistently follow geometries close to the transition state. This is consistent with the marked backward scattering observed in O($^3$P) reactions with larger hydrocarbons[53,54] or with smaller molecules such as $H_2$,[33] and it also follows the general trend for a number of triatomic reactions that exhibit collinear saddle points.[55]

Finally, angular distributions for the H + $OCH_3$ channel as a function of collision energy are depicted in Figure 8. Interestingly, at $E_{coll}$ = 2.36 eV, a bimodal distribution corresponding to the two different possible mechanisms that follow the two saddle points in Figure 6 can be inferred. There is a rather sharp backward peak that corresponds to the $SN_2$ mechanism and dominates over the flux scattered sideways corresponding to saddle point TS2. At higher energies, the distinction between the two mechanisms fades, and the angular distributions become essentially independent of collision energy.

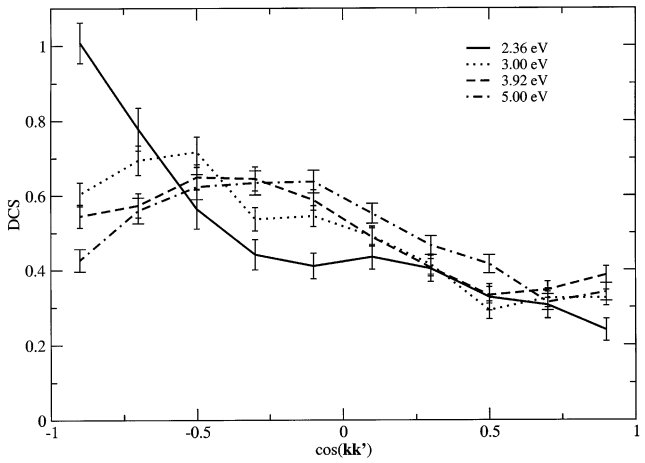


**Figure 8.** Angular distributions for the O($^3$P) + $CH_4$→ H + $OCH_3$ reaction for various translational energies expressed as normalized differential cross sections (DCS, $(2\pi/\sigma)(d\sigma/d\Omega')$). All of the calculations correspond to the MSINDO potential energy surface.

## IV. Concluding Remarks

We have carried out an extensive study of the O($^3$P) + $CH_4$ reaction, emphasizing the reaction dynamics at several electronvolt collision energies that would be important to low Earth orbit materials erosion experiments. Reaction dynamics studies have been carried out in full dimensionality employing the quasiclassical trajectory method and using four expressions for the potential energy: an analytical potential energy surface from the literature, semiempirical PM3 calculations, semiempirical MSINDO calculations, and B3LYP/6-31G* calculations.

Comparing these methods with coupled-cluster theory for the reaction energies and barriers shows the expected trends, with MSINDO calculations noticeably improving over PM3 but without the drastic increase in computation time needed for more accurate techniques.

The analysis of the cross sections reveals that the lowest barrier products, OH + $CH_3$, are not dominant at high energies. Instead, H + $OCH_3$ is more important, even though the barrier for this channel is greater than 1.75 eV. There is also a non-negligible cross section for the production of $CH_2O$ + 2H. These findings have important consequences for materials erosion in LEO. Structural damage following reactions between fast oxygen atoms and hydrocarbon surfaces is going to be more important in reactions where H atoms are exchanged with oxygen atoms than in those that generate OH. This is because H-elimination reactions lead to carbon−oxygen bond formation, thereby providing a path to carbonyl formation and ultimately to the production of volatile products such as CO and $CO_2$. Note also that all of the calculations in this paper have been concerned with the triplet state of oxygen, so the present results indicate that effective pathways for forming C−O bonds that do not require intersystem crossing to the singlet state during reaction are possible.

Energy release to the OH + $CH_3$ products preferentially goes into translation, with OH being vibrationally and rotationally cold in our best results. Rotational excitation is shown to be sensitive to the loose bending-energy curves of the semiempirical and analytical potentials such that only the B3LYP results give the correct (cold) behavior. The $CH_3$ energy is barely above the zero-point energy at all translational energies. However, the analysis of the H + $OCH_3$ channel shows large internal excitation in the polyatomic product and a decreased release to translation as a result of the distinct kinematics.

Angular distributions for the reaction show OH + $CH_3$ being more and more forward scattered as collision energy is increased, as would be expected for a direct reaction. The analysis of opacity functions clearly indicates that trajectories reacting with low impact parameters yield H + $OCH_3$ in preference to OH + $CH_3$, thereby enhancing the forward peak of the OH + $CH_3$ distribution. The H + $OCH_3$ angular distributions are broader but predominantly backward. Angular distributions at energies close to the threshold for this channel reflect the presence of two different reaction paths.

Methodologically, what we learn from this study is that a novel semiempirical technique, MSINDO, shows reasonable accuracy with very competitive computation times. We find that the MSINDO energies are noticeably better than the PM3 energies when compared with higher-accuracy methods. Also, MSINDO is the semiempirical technique that overall compares best with more accurate techniques in the reaction dynamics results, even for the high-barrier products.

Customarily, the PM3 Hamiltonian has been reparametrized according to the specifics of a given reaction before it is able to provide useful results. We show here that MSINDO gives reasonable results for high-energy collision simulations without parameter optimization. However, caution should be used when employing this technique for low-energy calculations, where dynamics properties such as product rotation are more sensitive to inaccuracies in the potential. Further calculations on different systems should verify the suitability of MSINDO for dynamics calculations.

**Acknowledgment.** This research was supported by AFOSR MURI grant F49620-01-1-0335 and by NSF grant CHE-0131998. We acknowledge Thomas Bredow for his prompt help with the MSINDO code and G. Lendvay for his help in interfacing molecular dynamics routines with MSINDO. This work was also partially supported by the National Computational Science Alliance under grant CHE020037N.

## References and Notes

(1) Champion, K. S. W.; Cole, A. E.; Kantor, A. J. In *Handbook of Geophysics and the Space Environment*; Jursa, A. S., Ed.; Air Force Geophysics Laboratory, Air Force Systems Command, United States Air Force, 1985.

(2) Banks, B. A.; Groth, K. K. d.; Rutledge, S. L.; DiFilippo, F. J. *Prediction of In−Space Durability of Protected Polymers Based on Ground Laboratory Thermal Energy Atomic Oxygen*; NASA: Washington, DC, 1996.

(3) Murad, E. *J. Spacecr. Rockets* **1996**, *33*, 131.

(4) Garton, D. J.; Minton, T. K.; Troya, D.; Pascual, R. Z.; Schatz, G. C. *J. Phys. Chem. A* **2003**, *107*, 4583.

(5) Minton, T. K.; Garton, D. J. Dynamics of Atomic-Oxygen-Induced Polymer Degradation in Low Earth Orbit. In *Advanced Series in Physical Chemistry: Chemical Dynamics in Extreme Environments*; Dressler, R. A., Ed.; World Scientific: Singapore, 2001; p 420.

(6) Warnatz, J. *Combustion Chemistry*; Springer-Verlag: Berlin, 1984.

(7) Sutherland, J. W.; Michael, J. V.; Klemm, R. B. *J. Phys. Chem.* **1986**, *90*, 5941.

(8) Cohen, N.; Westberg, K. R. *J. Phys. Chem. Ref. Data* **1991**, *20*, 1211.

(9) Baulch, D. L.; Cobos, C. J.; Cox, R. A.; Esser, C.; Frank, P.; Just, T. H.; Kerr, J. A.; Pilling, M. J.; Troe, J.; Walker, R. W.; Warnatz, J. *J. Phys. Chem. Ref. Data* **1992**, *21*, 445.

(10) Suzuki, T.; Hirota, E. *J. Chem. Phys.* **1993**, *98*, 2387.

(11) Sweeney, G. M.; Watson, A.; McKendrick, K. G. *J. Chem. Phys.* **1997**, *106*, 9172.

(12) Ausfelder, F.; McKendrick, K. G. *Prog. Reac. Kinet. Mech.* **2000**, *25*, 299.

(13) Jursic, B. S. *Int. J. Quantum Chem.* **1997**, *65*, 75.

(14) Corchado, J. C.; Espinosa-Garcia, J.; Roberto-Neto, O.; Chuang, Y.-Y.; Truhlar, D. G. *J. Phys. Chem. A* **1998**, *102*, 4899.

(15) Gonzalez, M.; Hernando, J.; Millan, J.; Sayos, R. *J. Chem. Phys.* **1999**, *110*, 7326.

(16) Roberto-Neto, O.; Machado, F. B. C.; Truhlar, D. G. *J. Chem. Phys.* **1999**, *111*, 10046.

(17) Espinosa-Garcia, J.; Garcia-Bernaldez, J. C. *Phys. Chem. Chem. Phys.* **2000**, *2*, 2345.

(18) Jordan, M. J. T.; Gilbert, R. G. *J. Chem. Phys.* **1995**, *102*, 5669.

(19) Sayos, R.; Hernando, J.; Puyuelo, M. P.; Enriquez, P. A.; Gonzalez, M. *Chem. Phys. Lett* **2001**, *341*, 608.

(20) Palma, J.; Clary, D. C. *Phys. Chem. Chem. Phys.* **2000**, *2*, 4105.

(21) Wang, M.-L.; Li, Y.-L.; Zhang, J. Z. *J. Phys. Chem. A* **2001**, *105*, 2530.

(22) Yu, H.-G.; Nyman, G. *J. Chem. Phys.* **2000**, *112*, 238.

(23) Palma, J.; Clary, D. C. *J. Chem. Phys.* **2001**, *115*, 2188.

(24) Huarte-Larrañaga, F.; Manthe, U. *J. Chem. Phys.* **2002**, *117*, 4635.

(25) Stewart, J. J. P. *J. Comput. Chem.* **1989**, *10*, 209.

(26) Schmidt, M. W.; Baldridge, K. K.; Boatz, J. A.; Elbert, S. T.; Gordon, M. S.; Jensen, J. J.; Koseki, S.; Matsunaga, N.; Nguyen, K. A.; Su, S.; Windus, T. L.; Dupuis, M.; Montgomery, J. A. *J. Comput. Chem.* **1993**, *20*, 1347.

(27) Ahlswede, B.; Jug, K. *J. Comput. Chem.* **1999**, *20*, 563.

(28) Jug, K.; Geudtner, G.; Homann, T. *J. Comput. Chem.* **2000**, *21*, 974.

(29) Bredow, T.; Geudtner, G.; Jug, K. *J. Comput. Chem.* **2001**, *22*, 89.

(30) Becke, A. D. *J. Chem. Phys.* **1993**, *98*, 5648.

(31) Lee, C.; Yang, W.; Parr, R. G. *Phys. Rev. B* **1988**, *37*, 785.

(32) Rogers, S.; Wang, D.; Kupperman, A.; Walch, S. *J. Phys. Chem. A* **2000**, *104*, 2308.

(33) Garton, D. J.; Minton, T. K.; Maiti, B.; Troya, D.; Schatz, G. C. *J. Chem. Phys.* **2003**, *118*, 1585.

(34) Curtiss, L. A.; Kock., L. D.; Pople, J. A. *J. Chem. Phys.* **1991**, *95*, 4040.

(35) Knowles, P. J.; Hampel, C.; Werner, H.-J. *J. Chem. Phys.* **1993**, *99*, 5219.

(36) Dunning, T. H., Jr. *J. Chem. Phys.* **1989**, *90*, 1007.

(37) Kong, J.; White, C. A.; Krylov, A. I.; Sherrill, C. D.; Adamson, R. D.; Furlani, T. R.; Lee, M. S.; Lee, A. M.; Gwaltney, S. R.; Adams, T. R.; Ochsenfeld, C.; Gilbert, A. T. B.; Kedziora, G. S.; Rassolov, V. A.; Maurice, D. R.; Nair, N.; Shao, Y.; Besley, N. A.; Maslen, P. E.; Dombroski, J. P.; Dachsel, H.; Zhang, W. M.; Korambath, P. P.; Baker, J.; Byrd, E. F. C.; Voorhis, T. V.; Oumi, M.; Hirata, S.; Hsu, C. P.; Ishikawa, N.; Florian, J.; Warshel, A.; Johnson, B. G.; Gill, P. M. W.; Head-Gordon, M.; Pople, J. A. *Q-Chem*, version 2.0; Q-Chem, Inc.: Export, PA, 2000.

(38) DeMore, W. B.; Sander, S. P.; Golden, D. M.; Hampson, R. F.; Kurylo, M. J.; Howard, C. J.; Ravishankara, A. R.; Kolb, C. E.; Molina, M. J. *Chemical Kinetics and Photochemical Data for Use in Stratospheric Modeling*; Evaluation No. 11, JPL Publication 94-26; NASA Panel for Data Evaluation, Jet Propulsion Laboratory; California Institute of Technology: Pasadena, CA, 1994.

(39) Gonzalez-Lafont, A.; Truong, T. N.; Truhlar, D. G. *J. Phys. Chem.* **1991**, *95*, 4618.

(40) Li, G.; Bosio, S. B. M.; Hase, W. L. *J. Mol. Struct.* **2000**, *556*, 43.

(41) Taketsugu, T.; Gordon, M. S. *J. Phys. Chem.* **1995**, *99*, 14597.

(42) Troya, D.; Gonzalez, M.; Schatz, G. C. *J. Chem. Phys.* **2001**, *114*, 8397.

(43) Troya, D.; Lakin, M. J.; Schatz, G. C.; Harding, L. B.; Gonzalez, M. *J. Phys. Chem. B* **2002**, *106*, 8148.

(44) Zhang, J.; Garton, D. J.; Minton, T. K. *J. Chem. Phys.* **2002**, *117*, 6239.

(45) McFarlane, J.; Polanyi, J. C.; Shapter, J. G. *J. Photochem. Photobiol., A* **1991**, *58*, 139.

(46) Schatz, G. C.; Amaee, B.; Connor, J. N. L. *J. Chem. Phys.* **1990**, *92*, 4893.

(47) Troya, D.; Millan, J.; Baños, I.; Gonzalez, M. *J. Chem. Phys.* **2002**, *117*, 5730.

(48) Andresen, P.; Luntz, A. C. *J. Chem. Phys.* **1980**, *72*, 5842.

(49) Strazisar, B. R.; Lin, C.; Davis, H. F. *Science* **2000**, *290*, 958.

(50) Lakin, M. J.; Troya, D.; Lendvay, G.; Gonzalez, M.; Schatz, G. C. *J. Chem. Phys.* **2001**, *115*, 5160.

(51) Troya, D.; Gonzalez, M.; Wu, G.; Schatz, G. C. *J. Phys. Chem. A* **2001**, *105*, 2285.

(52) Levine, R. D.; Bernstein, L. B. *Molecular Reaction Dynamics and Chemical Reactivity*; Oxford University Press: New York, 1987.

(53) Liu, X.; Gross, R. L.; Hall, G. E.; Muckerman, J. T.; Suits, A. G. *J. Chem. Phys.* **2001**, *117*, 7947.

(54) Liu, X.; Gross, R. L.; Suits, A. G. *J. Chem. Phys.* **2002**, *116*, 5341.

(55) Pascual, R. Z.; Schatz, G. C.; Lendvay, G.; Troya, D. *J. Phys. Chem. A* **2002**, *106*, 4125.